Multistate Tuning of Third Harmonic Generation in Fano-Resonant Hybrid Dielectric Metasurfaces

Omar A. M. Abdelraouf [1,3], Aravind P. Anthur[3], Zhaogang Dong[3], Hailong Liu[3], Qian Wang[3], Leonid Krivitsky[3], Xiao Renshaw Wang[1,2]*, Qi Jie Wang[1,2,]*, Hong Liu[3,]*

Affiliations:
[1]School of Physical and Mathematical Sciences, Nanyang Technological University, Singapore 637371, Singapore
[2]School of Electrical and Electronic Engineering, 50 Nanyang Avenue, Nanyang Technological University, Singapore 639798, Singapore
[3]Institute of Materials Research and Engineering, Agency for Science, Technology and Research (A*STAR), 2 Fusionopolis Way, #08-03, Innovis, Singapore 138634, Singapore

*To Whom correspondence should be addressed. Email: renshaw@ntu.edu.sg, qjwang@ntu.edu.sg, h-liu@imre.a-star.edu.sg

ABSTRACT
Hybrid dielectric metasurfaces have emerged as a promising approach to enhancing near field confinement and thus high optical nonlinearity by utilizing low loss dielectrics rather than relatively high loss metallic resonators. A wider range of applications could be realized if more design dimensions can be provided from material and fabrication perspectives to allow dynamic control of light. Here, we demonstrate an efficient and tunable third harmonic generation (THG) via hybrid metasurfaces with phase change material $Ge_2Sb_2Te_5$ (GST) deposited on top of amorphous silicon metasurfaces. Fano resonance is excited to confine the incident light inside the hybrid metasurfaces, and an experimental quality factor (*Q*-factor ~ 125) is achieved at the fundamental pump wavelength around 1210 nm. We have demonstrated not only the switching between a turn-on state of Fano resonance in the amorphous state of GST and a turn-off state in its crystalline state, but also gradual multistate tuning of THG emission at its intermediate state. A high THG conversion efficiency of $\eta = 2.9 \times 10^{-6}$ % has been achieved, which is more than ~32 times that of a GST-based Fabry-Pèrot cavity under a similar pump laser power, thanks to the enhanced field confinement at the Fano resonance. These results show the high potential of exploring GST-based hybrid dielectric metasurfaces for highly efficient and tunable nonlinear optical devices.

Keywords: Multistate tuning, Fano resonance, hybrid metasurfaces, GST, phase change, third harmonic generation

INTRODUCTION

Third harmonic generation (THG) is a common nonlinear optical phenomenon,[1] which generates photons with triple frequencies of those of the incident photons. One advantage of THG over second harmonic generation (SHG) is that it can be generated from nonlinear materials with arbitrary lattice structures. THG has been used in many applications, such as imaging of lipid bodies in tissues,[2] generating free-electron laser in the near infrared (NIR),[3] probing quantum tunneling limit in self-assembled monolayer,[4] spectroscopy,[5] light modulation,[6] nonlinear optical image encoding,[7] and its tunability has been explored in light modulation of generated harmonics.[8] Motivated by those applications, it is highly desirable to improve the conversion efficiency of THG and to modulate its emission amplitude in tunable nonlinear optical devices.

Nonlinear crystals have been widely utilized for generating THG. However, they are expensive, bulky, and have stringent phase matching conditions between the fundamental and the generated harmonic fields. On the other hand, metasurfaces, namely artificially engineered nanostructures, have been utilized to confine the incident light down to a subwavelength scale to enhance THG. In addition, metasurfaces do not require the stringent phase matching conditions for high-order harmonic generation (HHG). Plasmonic metasurfaces consisting of metallic nanostructures have been used for THG via a variety of structures such as gap plasmon,[9] multi quantum well,[10] and toroidal dipole plasmonic meta-atom.[11] Generally, the light confinement via plasmonic metasurfaces is constrained to only over the surface of metals. Moreover, the intrinsic Ohmic losses of metals reduce both conversion efficiency and the damage threshold of plasmonic metasurfaces.

In contrast, owing to their high permittivity and inherent low optical losses, dielectric metasurfaces have been proposed to overcome the issue of Ohmic losses of metallic metasurfaces.[12–14] The modes of the incident light are confined in the whole volume of dielectric nanostructures, which greatly enhance the conversion efficiency of THG. In addition, dielectric metasurfaces have relatively higher damage thresholds, which outperform their plasmonic counterparts. Recently, dielectric metasurfaces have been extensively studied to enhance the efficiency of THG and other HHGs in nonlinear

dielectric nano-resonators driven by high Q-factor Fano-resonance,[15–18],[19,20] anapole resonance,[21–24] and bound states in the continuum (BIC).[25–27] Recently, reconfigurable metasurfaces have been developed to realize active tuning of various functions upon different stimuli.[28,29] For example, it can be achieved via tuning refractive index of liquid crystals by manipulating their molecules rotation,[30] using optical pumping to tune free carriers generation in semiconductors,[31] or applying an electrical bias to tune Fermi energy level in graphene.[32]

Among the tunable materials utilized in the reconfigurable metasurfaces, optical phase change materials (PCMs) stand out by their giant optical property contrast upon a solid state phase transition between amorphous and crystalline states. Such giant optical contrast comes from the different bonding mechanisms at these two states. At the amorphous state, PCMs undergo covalent bonding with substantial valence between neighboring atoms. In contrast, PCMs undergo a shift to resonant bonding at the crystalline state.[33] Different bonding mechanisms in PCMs are very stable, enabling their applications in non-volatile rewritable memory. Another advantage of PCMs is the fast and reversible transition between those two states, upon external optical, electrical, or thermal stimulus.[34] PCMs consist of different compounds, such as sulfide (S), selenide (Se), and telluride (Te). Different combinations of PCMs compounds provide the ability to tune the optical properties of PCMs from low loss material to high loss material or even metallic-like material at different wavelength ranges.

Integrating phase change materials (PCMs) in hybrid dielectric metasurfaces offers non-volatile phase change between amorphous and crystalline states, ultrafast switching speed, broadband and large tuning of the refractive index and compatibility with the CMOS technology.[35–37] A Fabry-Pèrot cavity in reflection mode based on high refractive index $Ge_2Sb_2Te_2$ (GST) has been demonstrated to achieve two-state switching (ON/OFF) of THG.[38] However, its THG conversion efficiency is only about 5.46×10^{-9} %, which is largely attributed to the low Q-factor of the device and inherent high optical losses in the thick GST film.

In this work, we design a transmissive mode hybrid metasurfaces consisting of amorphous silicon and GST nanostructures, and experimentally realize gradual tuning of the amplitude of THG. The high nonlinearity in silicon nanostructures generates third harmonic emission, while multiple phase states of GST control the emitted THG intensity.[39,40] Fano resonance subsequently enhances the light confinement inside the silicon nanostructures, which greatly improves THG conversion efficiency. We achieved a THG enhancement factor of ~128 compared to an unpatterned GST-Si thin film and a corresponding conversion efficiency of up to $2.9 \times 10^{-6}\%$ at a pump power of 55 mW. The measured conversion efficiency is ~32 times higher than that of the GST-based Fabry-Pèrot cavity using a similar pump laser power density.[38] The tunability of THG amplitude was realized via the gradual phase change among the amorphous, intermediate and crystalline states of the GST nanostructures.

RESULTS AND DISCUSSION

Figure 1 illustrates the design concept of tunable THG using hybrid silicon-GST metasurfaces, which consist of two split-ring resonators (SRR) connected to each other as shown in Fig. 1a. The advantage of adopting SRR structures is to achieve a very high Q-factor Fano resonance comparable with other types of resonant structures demonstrated in the literature.[41] Through the simulation, we have optimized the design parameters of SRR structures, such as period, height, side wall and air gap width, which enables us to control the interference between the electric and magnetic modes formed inside SRR structures. In addition, we can sweep the structural design parameters systematically to obtain the optimized Q-factor at the desired wavelength. The width of the middle rod (w_1) and the outer rod width (w_2) are optimized to be 200 nm and 120 nm, respectively, to maximize the Q-factor of Fano resonance (see Fig. S1 in the supporting information, SI). The silicon SRR structure enhances the field confinement and hence the Q-factor of the Fano resonance, which is induced by breaking the symmetry of SRR of the hybrid metasurfaces. The incident light is perpendicular to the sample surface (*x*-*y* direction) and its polarization is along the *y*-axis to excite the Fano resonance. Other structural parameters of SRR on quartz are shown in Fig. 1b. A 5-nm thick GST layer on top of the silicon SRR enables both tunable THG in transmission mode and tunable Fano resonance in the silicon SRR. Details about the GST thickness layer optimization are provided in SI. Nanofabrication process of

the proposed hybrid metasurfaces started from electron beam lithography (EBL) followed by inductively coupled plasma-reactive ion etching (ICP-RIE) using hydrogen silsesquioxane (HSQ) as an etching mask. A scanning electron microscope (SEM) image of the fabricated hybrid metasurfaces is shown in Fig. 1c and its inset shows the SEM image of the unit cell. For more details on fabrication steps see Methods section and Fig. S4 in the SI.

The phase change of GST can be excited upon annealing of samples on a hotplate at a temperature above its phase-change temperature. Baking GST film at ~ 180 °C and ~ 300 °C for a few minutes will transform it into an intermediate state and full crystalline state, respectively. Intermediate states of GST film are formed due to the co-existence of the cubic phase and the hexagonal phase with different ratios, while a full crystalline state results from a pure hexagonal phase.[36] We quantitatively investigated the variation of optical properties of GST at the multiple phase states by measuring the refractive index (n) and extinction coefficient (k) of GST film using variable angle spectroscopic ellipsometry (JA Woollam VB400). The fitting was carried out by using the Tauc-Lorentz model and the mean square error (MSE) of less than 20 was achieved for all measurements. The measured refractive index and extinction coefficient are plotted in Figs. 1d and 1e, respectively. It can be observed that the refractive index gradually increases with the annealing time. At the wavelength of ~ 1200 nm, the changes in refractive index (Δn) of ~ 0.68 and 0.79 were measured after annealing at a temperature of 180 ^{o}C for 2 and 4 minutes, respectively. Similarly, the extinction coefficient gradually increases from an amorphous state (a-GST) to intermediate states (i-GST) and finally reaches the highest value at the full crystalline state (c-GST). The corresponding changes of extinction coefficient (Δk) were ~ 0.50 and 0.61, respectively. Multiple i-GSTs can be achieved via increasing the annealing time. Upon c-GST, a very large value of Δn of ~ 3.15 and extinction coefficient k of ~ 2.38 at wavelength 1200 nm were measured, which agreed well with the literature.[42] Moreover, our results provide rich data sources of the optical properties of GST, which offers more design freedom for multi-functional metasurfaces based on GST. To test the quality of c-GST film, we did Raman spectroscopy measurement on a sample with sputtered GST film

(5 nm thickness) on quartz, (Fig. S6). The measured Raman spectra of a-GST and c-GST films agree with the literature.[43]

Figure 2 shows the simulated and measured results verifying the multistate tunability of Fano-resonance in the hybrid dielectric metasurfaces. Figure 2a shows a sharp peak of Fano resonance formed at the wavelength of 1292.6 nm in the simulated transmission spectrum of a-GST. Due to the low optical loss at a-GST, it leads to the strongest Fano-resonance and the highest Q-factor. As a result, a high transmission of ~ 72% at the Fano resonance wavelength is achieved, which denotes the "turn-on" state of the device. Fano resonance facilitates at a high Q-factor of ~ 615 corresponds to a full width at half maximum (FWHM) of around 2.1 nm. The dip depth of Fano resonance is around 38%, which was measured through the amplitude difference between the maximum and the minimum transmission at the Fano resonance wavelength. The calculated dephasing time (t_d) is approximately 245 femtosecond (fs). More details about the dephasing time calculation can be found in the SI. For the intermediate state achieved after annealing the sample at 180^{o}C for 2 minutes, the dip depth reduces to 28%. The FWHM of Fano resonance increases to 2.4 nm, while the Fano resonance wavelength redshifts to 1292.9 nm, and the dephasing time reduces to ~160 fs. After 4 minutes of annealing, the dip depth is further reduced to 8%. The FWHM of Fano resonance increases to 5.6 nm while the resonance wavelength redshifts to 1294.6 nm with a longer decay in the dephasing time of 95 fs. At i-GST, the FWHM of Fano resonance increases with the annealing time, which shows the Fano-resonance becomes weaker due to the increase of the optical loss in GST film. The i-GST denotes the "dynamic tuning" state of the device since its optical properties gradually vary with the phase change upon annealing. The full crystalline state was achieved by annealing the sample at 300 ^{o}C for 5 minutes,[44] and there is no resonance observed for c-GST, besides vanishing of the dephasing time. The highest optical loss in c-GST state is detrimental to the excitation of Fano resonance so that the hybrid metasurfaces cannot function for the THG enhancement, which denotes the "turn-off" state of the device. All simulations were carried out using the measured refractive index of amorphous silicon and GST at different states. In addition, we calculated the modal volume (V_e) to assess the light-matter interaction within the SRR cavity. At the a-GST, the V_e is 0.0135 μm^3 at Fano resonance dip wavelength (as shown in Fig. S2). The small modal volume and high Q-factor resonance indicate a strong light

localization within the cavity.[45] For the i-GST state (after 2 min of annealing), the amplitude of V_e drops to 0.0125 μm^3 and Q-factor reduces to ~538, which indicates a lower light coupling within the cavity. At the c-GST state, the Q-factor is vanished, and the incident light cannot couple to the SRR cavity. More details and discussion about modal volume calculations are provided in the SI.

Correspondingly, the measured transmission spectrum is shown in Fig. 2b. The curve of a-GST exhibits Fano resonance wavelength at 1211.8 nm with FWHM of 9.7 nm**,** t_d of 160 fs and a dip depth is 24%. The measured Q-factor was ~ 125, which is smaller than the simulated value possibly due to the device fabrication mismatch. The degradation in the Fano resonance of the fabricated sample is largely due to the nanofabrication imperfection, in particular, a small variation of side wall width significantly blueshifts the Fano resonance wavelength. At i-GST, the dip depth of Fano resonance gradually reduced from 17% to 7% when the annealing time rose from 2 mins to 4 mins; at the same time. We observed that the FWHM of the Fano resonance curve increased from ~10.3 nm to 12.5 nm, while t_d decreased from 150 fs to 124 fs correspondingly. The Fano resonance completely vanished at c-GST state, which is identical to the theoretical prediction. The dip depth of the Fano resonance gradually reduced from a-GST to i-GST till it became zero at the c-GST with a measured transmission of ~55%.

To investigate the origin of Fano-resonance, the multipolar decomposition method has been implemented individually using the finite difference time domain (FDTD) method for each GST state and the simulated results are shown in Figs. 2c to 2e, respectively. In the case of a-GST as shown in Fig. 2c, the total scattering cross section has strong electric quadrupole (*EQ*) resonance with FWHM of ~ 2.4 nm, while electric dipole (*ED*) shows damped oscillation with a very small normalized magnitude less than 0.028. Therefore, the Fano resonance in the proposed hybrid metasurfaces arises from a destructive interference between in-plane damped electric dipole which oscillates in *y*-direction (ED_y) and out-of-plane high Q-factor electric quadrupole in *z*-direction (EQ_z). In the case of i-GST after 2 minutes of annealing, the normalized scattering cross section shows larger an FWHM (3.17 nm) of EQ_z curve than that of a-GST. Meanwhile, the peak EQ_z scattering degrades as well

by 33%. ED_y maintains a small scattering magnitude of less than 0.015. That explains the origin of relatively weak Fano-resonance at i-GST. Upon full crystallization, it shows that total normalized scattering efficiency has been reduced significantly to ~ 0.12 as compared with a-GST. No resonance is observed for all modes and that results in the high transmission at Fano resonance wavelength formed in a-GST, which agrees well with the measured transmission of the metasurfaces.

Figures 2f to 2h show the simulated results of normalized total electric field intensity of a-GST, i-GST (2 mins) and c-GST, respectively. In each figure, the normalized electric field profile of *x*-*y* (horizontal) plane at a position of *z*=200 nm is shown in the left plot while the normalized electric field profile of the *y*-*z* (vertical) plane at the center of unit cell is illustrated in the right plot. In the case of a-GST, the field distribution shows high field confinement in electric quadrupole (*EQ*) mode with out-of-plane field oscillations. While another electric dipole (*ED*) mode oscillates horizontally along the central air gap. For the i-GST (2 min), the corresponding normalized field distribution shows field vectors of *EQ* and *ED* similar to a-GST. However, the intensity of field confinement of i-GST is reduced to 67% of a-GST due to the relatively higher optical losses in i-GST film, which results in a weaker Fano resonance. In addition, the field distribution shows the vanishing of *EQ* at c-GST, indicating there is no out-of-plane field oscillation. Meanwhile, the maximum field intensity is decreased to 29% compared with a-GST. The field distribution and the multipolar scattering of c-GST agree in terms of vanishing resonant modes near Fano resonance wavelength at a-GST.

The vertical slice (*y*-*z* plane) in the case of a-GST, shows confinement of the electric field in the air gap. Rotation of the electric dipole field vector between the top Si-GST interface and the bottom Si-quartz interface satisfies the continuity equation of lateral electric field intensity. The field distribution for the i-GST is similar to a-GST but its amplitude of peak field is reduced to 67%. For c-GST, the electric field vector along the central air gap reverses its direction due to the giant refractive index change of GST film. Moreover, the giant optical losses in c-GST state reduce the amplitude of peak localized electric field to 32% compared to a-GST.

To experimentally measure the near field enhancement achieved by Fano resonance, we used a home-built optical setup. The femto-second laser beam was generated from an optical parametric oscillator (APE) with a pulse width of 200 fs and a tunable range of 1100 ~ 1300 nm in Fig. 3a. The incident light was focused on the sample using plano-convex lens with a focal length of 25.4 mm. The diameter of focused laser beam spot was 15 μm. Transmitted THG was collected by an objective with 0.55 numerical aperture (NA) and filtered by a low pass UV filter before being coupled to a spectrometer (Ocean Optics, USB4000). Details of the optical setup can be referred to Methods section and Fig. 3a.

Figure 3b shows the measured optical characterization of THG at a-GST. We observed a THG peak at the wavelength of ~ 404 nm, corresponding to the fundamental incident wavelength of ~ 1216 nm. It indicates that the enhancement of THG emission comes from the enhanced localized near field inside hybrid metasurfaces at the Fano resonance wavelength as shown in Fig. 3a. Moreover, the emission peak wavelength is nearly one-third of the Fano resonance peak wavelength, indicating that emitted field is THG. We further examined the polarization dependence of THG emission by varying the pump laser polarization via a half-wave plate (HWP). Figure 3c plots the variation of the measured intensity of THG emission with the pumped laser polarization. The enhancement of THG emission vanishes under the perpendicular incident polarization (*x*-direction). It is consistent with our design depicted in Fig. 1 that Fano resonance is only able to be excited by the *y*-polarized pump laser. The far field emission of THG was measured using 4f-lens setup to get a back focal plane (BFP) image using a CCD camera and the measured diffraction patterns are plotted in Fig. 3d. The integration time used in the measured BFP image is calibrated to avoid color saturation. The detected intensity of the higher-order diffraction is lower than that of the zero-order diffraction, which indicates the feasibility of collecting most of THG emission from the proposed hybrid metasurfaces for practical applications using low NA lenses.

The measurement and characterization results of the tunability of THG are plotted in Fig. 4. We measured the THG spectrum at each state of GST and fixed the output power of the

laser to the maximum of ~55 mW, which was equivalent to a peak power density of up to 1.6 GW/cm^2 as shown in Fig. 4a. At a-GST, the intensity of THG emission reached its maximum at the peak wavelength of ~ 404 nm. After annealing for 2 minutes, the measured THG emission was degraded. That could be explained by the weaker Fano resonance after annealing as shown in Fig. 2b. When the annealing time increased to 4 minutes, it was observed that emitted THG was further decreased due to the smaller light confinement of the very weak Fano resonance. For c-GST, no THG emission was detected which indicates that thin GST film has undergone a complete phase change and there was no observation of Fano resonance. The modulation depth (MD) of the designed hybrid metasurface can be calculated through.

$$MD = \frac{|I_{max} - I_{min}|}{I_{max}} \quad (1)$$

where I_{max} and I_{min} are the maximum and minimum THG intensity, respectively. By excluding the background noise of the THG signal, we achieved MD of ~65 % for i-GST (2 min), ~78% for i-GST (4 min), and ~100% for c-GST states. The measured MD results show the potential for efficient modulation of THG intensity. We performed the nonlinear optical simulations to estimate the relative change in THG intensity as shown in Fig S7. The calculated MD is 66% for i-GST (2 min) and 98% for c-GST states, respectively. More details about the nonlinear optical calculations can be found in the SI.

We also measured the THG power dependence on the pump power at each state of GST. Figure 4b shows the variation of the measured THG power with pump powers. It can be observed that the highest THG power of up to 1.6 nW at the pump power of 55 mW was achieved at the a-GST. That corresponds to a THG enhancement factor of ~125 in respect of an unpatterned GST-Si film. Our THG conversion efficiency was calculated based on the following equation:

$$\eta = \frac{P_{THG}}{P_{pump}} = 2.9 \times 10^{-6}\ \%. \quad (2)$$

The experimentally measured THG conversion efficiency is ~32 times higher than the amplitude of THG emitted from the Fabry-Perot cavity incorporated with GST using the same pump laser power.[38] To fit the measured THG power, we used the power dependence formula $P_{THG} = aP^b{}_{Pump}$ with a line slope near 3. The line slope of 3 fits THG

power for a-GST state while the line slope of 3.1 fits i-GST with the annealing time of 2 min and 4 min, respectively. All the measured power points show R-squared values higher than 0.995 after fitting, which indicates that the measured power at each GST state is dominantly generated by THG. In addition, the measured THG power gradually decreased with annealing time, which indicates that the increase of optical losses in GST film at different states results in the degradation in the Fano resonance and reduction of the collected THG power.

CONCLUSION

In conclusion, we have demonstrated multistate tuning in THG emission using hybrid metasurfaces based on silicon-GST metasurfces. We employed silicon as a high dielectric constant and low loss material at the near-infrared regime to sustain Fano resonance to experimentally achieve a high Q-factor of up to 125 for THG emission enhancement. A thin layer of 5 nm thick phase change material of GST was deposited on top of Si metasurfaces to gradually tune the THG emission in transmission mode. THG conversion efficiency up to 2.9×10^{-6} % was achieved, which is ~32 times higher than a recent work based on GST-based Fabry-Pèrot cavity. Moreover, we have demonstrated multiple intermediate states of GST, which results in multilevel emission amplitude of THG. We believe that our tunable hybrid metasurfaces made of silicon-GST nanostructures pave the way for tunable nonlinear optics applications such as light modulation of HHGs in nonlinear materials, tunable lasing, and quantum entanglement.

METHODS

Transmission and Field Profile Simulations

Simulation of the proposed tunable silicon-GST hybrid dielectric metasurfaces was carried out using a finite difference time domain program (Lumerical FDTD Solutions) [46]. Three-dimensional simulation with periodic boundary condition in the lateral direction (*x*-*y* plane) and perfectly matched layer in the *z*-direction were adopted. The incident polarization was parallel to the middle rod of the structure (*y*-direction). The maximum mesh size was 10 nm for all simulation domains except phase change material of GST, which was smaller than 0.1 nm. The refractive indices of amorphous silicon and GST were measured from

their thin films deposited on a silicon substrate via ellipsometer and the results are plotted in Fig. S5 and Figs. 1d-1e in the main text, respectively. The refractive index of quartz was imported from Lumerical's database.

Multipolar Decomposition Simulations

The multipolar decomposition was simulated using two three-dimensional monitors in Lumerical FDTD, i.e., one for refractive index and the other for getting field components at each mesh. The scattering cross-sections of electric and magnetic modes were calculated using the following equations.

$$C_{ED} = \frac{k_0^4}{6\,\pi\epsilon_0^2 E_0^2}\left|p_{car} + \frac{ik_0}{c}\left(t + \frac{k_0^2}{10}\overline{R_t^2}\right)\right|^2 \quad (1)$$

$$C_{MD} = \frac{\eta_0^2 k_0^4}{6\,\pi E_0^2}\left|m_{car} - k_0^2\overline{R_m^2}\right|^2 \quad (2)$$

$$C_{EQ} = \frac{k_0^6}{80\,\pi\epsilon_0^2 E_0^2}\left|\overline{\overline{Q_e}} + \frac{ik_0}{c}\overline{\overline{Q_t}}\right|^2 \quad (3)$$

$$C_{MQ} = \frac{\eta_0^2 k_0^6}{80\,\pi E_0^2}\left|\overline{\overline{Q_m}}\right|^2 \quad (4)$$

Where C_{ED}, C_{MD}, C_{EQ}, C_{MQ} refers to scattering cross section of an electric dipole, magnetic dipole, electric quadrupole, and magnetic quadrupole, respectively. The scattering power formulas of electric dipole (P_{car}), toroidal dipole (t), magnetic dipole (m_{car}), electric quadrupole ($\overline{\overline{Q_e}}$), and magnetic quadrupole ($\overline{\overline{Q_m}}$) can be found in literature[47].

Fabrication of hybrid metasurface

Figure S3 schematically shows the fabrication flow process. Initially, the quartz substrate from (Photonik Singapore) was cleaned using acetone and isopropanol alcohol (IPA) in an ultrasonic bath for 5 min. A layer of ~400 nm thick amorphous silicon was deposited using inductively coupled plasma chemical vapor deposition (ICP-CVD, Oxford Plasmalab System 380) at a substrate temperature of 250 °C with RF power of 50 W, ICP power of 3000 W, silane and argon gases with flow of 45 and 30 sccm, respectively. 5 nm of phase change material of GST was deposited via an unbalanced magnetron sputtering under a power of 30 W, argon gas flow of 20 sccm, and chamber pressure of 4 mTorr. Hydrogen silsesquioxane (HSQ) was used as an etching mask for patterning the silicon metasurfaces using electron beam lithography (EBL, Elionix ELS-7000). SurPass 3000 was used as adhesion promoter followed by spin coating of HSQ (6%) at a speed of 2000 rpm for 60

sec to get the thickness of around 100nm. After that, EZspacer was spin-coated at 1500 rpm for 30 sec to avoid charging effect during EBL exposure, followed by nitrogen drying to remove excess EZspacer. EBL exposure was carried out under the conditions of the electron beam current of 500 pA, acceleration voltage of 100 kV, and dose charge 9600 uc/cm^2 to expose a field of 300 x 300 um^2 with 60,000 dots. After exposure, the sample was rinsed with deionized (DI) water to remove EZspacer layer, then developed in salty solution NaOH/NaCl (1:4) for 60 sec, followed by another 60 sec to rinse in DI water. After that sample was rinsed using IPA and then dried with nitrogen gas. Etching of silicon metasurfaces was implemented using inductively coupled plasma reactive ion etching (ICP-RIE, Oxford OIPT Plasmalab system) with HSQ as an etching mask. Etching gas consisted of chlorine with a flow of 22 sccm, using RF power of 200 W and ICP power of 400 W at room temperature. All measurements were done with a top residual HSQ layer of thickness ~ 40nm to protect GST from oxidation during the annealing process.

THG measurement

The optical setup used in this work is shown in Fig. 3a. Optical parametric oscillator (OPO) laser pumped via a Ti-Sapphire laser of wavelength 830 nm, with a repetition rate of around 76 MHz and pulse width of around 200 fs. The wavelength of OPO laser is tunable from 1100 nm to 1300 nm. Switching between OPO laser and ns-laser done with flipping mirror (M1). Variable attenuator used to examine the power slope of THG signal by changing the pump laser power. A quarter wave plate (QWP) was used to convert the elliptically polarized light to the linearly polarized light with a phase shift γ from the horizontal plane. A half-wave plate (HWP), attached to a motorized stage, was used to control the linearly polarized light to get the maximum power after passing through a linear polarizer (LP), which was used for measuring the polarization dependence of THG. A dichroic mirror was used to cut off light with wavelength shorter than 700nm. A lens (L1) of a focal length of 25.4 mm focused the laser beam on the sample. White light LED used to align laser spot on the fabricated pattern. The transmitted light was collected using an objective of 50x magnification and 0.55 numerical aperture (Mitutoyo Plan Apo). The collimated light was directed to a low pass filter (NE03A-A) with a cut-off wavelength above 400 nm. Flipping mirror (M2) switches between the back focal plane imaging of THG, THG spectrum, and

metasurfaces transmission at NIR. A set of mirrors (L2 to L4) used for back focal plane imaging. The spectrometer used for measuring THG spectrum was Ocean Optics (USB4000). For the diffraction measurement of THG signal, an objective x100 with numerical aperture 0.95 (Nikon Plan Apo) used to collect all diffracted THG signal.

Material characterization

The measured refractive index of amorphous silicon was fitted using Tauc-Lorentz model. Mean square error (MSE) for fitted data was lower than 10; the measured data was plotted in Fig. S5. To verify the phase change of a thin layer of GST (~5 nm, after annealing at a temperature of 300 ^{0}C for 5 minutes), we carried out the measurement of Raman spectra of both a-GST and c-GST and the results are plotted in Fig. S6a and S6b, respectively. A broad Raman scattering peak for a-GST centered near 140 cm^{-1}, while c-GST film shows a narrow peak centered near 117 cm^{-1}, which is consistent with the reported measurement of GST spectrum in literature,[43] which validates the phase change of the thin GST layer.

ASSOCIATED CONTENT

SUPPORTING INFORMATION

Additional simulation results of tuning Fano resonance with changing dimensions of the unit cell. GST thickness optimization tradeoffs, modal volume calculations inside SRR cavity, and equations used to calculate the dephasing time. The electric field maps inside GST film for amorphous, intermediate and crystalline states. Fabrication flow steps of proposed hybrid metasurfaces. The measured refractive index of amorphous silicon used in simulation. Measured Raman spectrum of GST film with 5-nm thickness for amorphous and crystalline states. Details of the nonlinear optical calculations.

AUTHOR CONTRIBUTIONS

O. A. M. A. proposed the idea and structure design, performed simulations, materials characterization, and nanofabrication. Optical characterization measurements were done by O. A. M. A. with help of A. P. A. who construct and align the THG setup. O. A. M. A. drafts the manuscript. All authors discussed and commented on the results and the

manuscript. X. R. W, Q. J. W., and L. H. convinced the idea, supervised the project and finalized the manuscript.

Competing Financial Interests
The authors declare no competing financial interest.

ACKNOWLOEDGMENT
This work is partially supported by Singapore Ministry of Education Academic Research Fund Tier 2 under grant no. MOE2018-T2-1-176, MOE-T2EP50120-006 and by A*STAR AME programmatic grant (grant no. A18A7b0058), IMRE project (SC25/18-8R1804-PRJ8), and AME IRG grant (Project No. A20E5c0094). Authors would like to thank DENG Jie, YAP Sherry, HUANG Aihong, Febiana Tjiptoharsono, and ANG Norman for their technical guide during optimization of nanofabrication processes. Also, Ramon Paniagua-Dominguez, and HO Jin Fa for their comments on multipolar decomposition results.

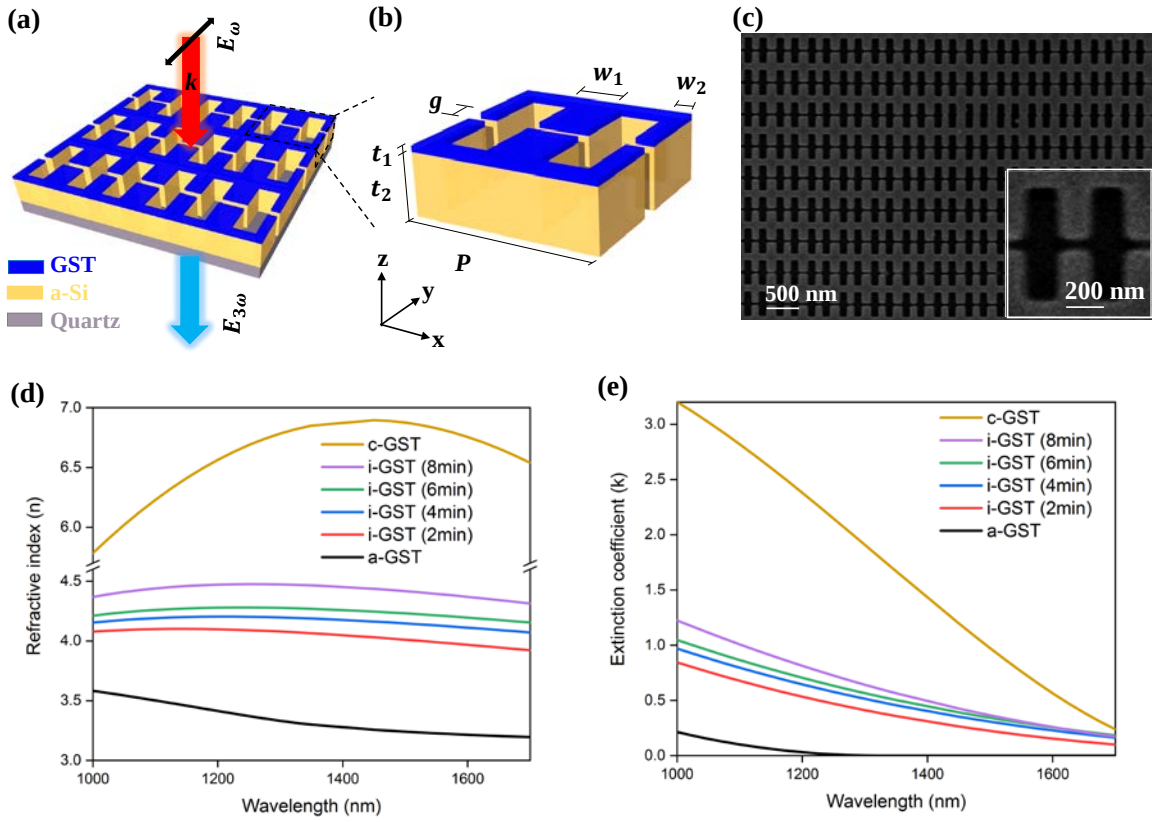

Figure 1. Schematics of the design of tunable THG via the hybrid silicon-GST metasurfaces. (a) Schematic of the proposed hybrid metasurfaces. The pump fs-laser (E_ω) and transmitted THG ($E_{3\omega}$) signals are denoted by red and blue arrows, respectively, where ω is the fundamental frequency. (b) Schematic of the hybrid metasurfaces unit cell with period p = 700 nm, GST thickness t_1 = 5 nm, silicon thickness t_2 = 400 nm, middle air gap g = 50 nm, middle rod width w_1 = 200 nm, and outer rod width w_2 = 120 nm. (c) SEM of the fabricated hybrid metasurfaces, and the inset shows the unit cell. (d) Measured real refractive index n for amorphous and crystalline GST, and different intermediate GST states after different annealing times at 180 ^{0}C. (g) Corresponding measured extinction coefficient k.

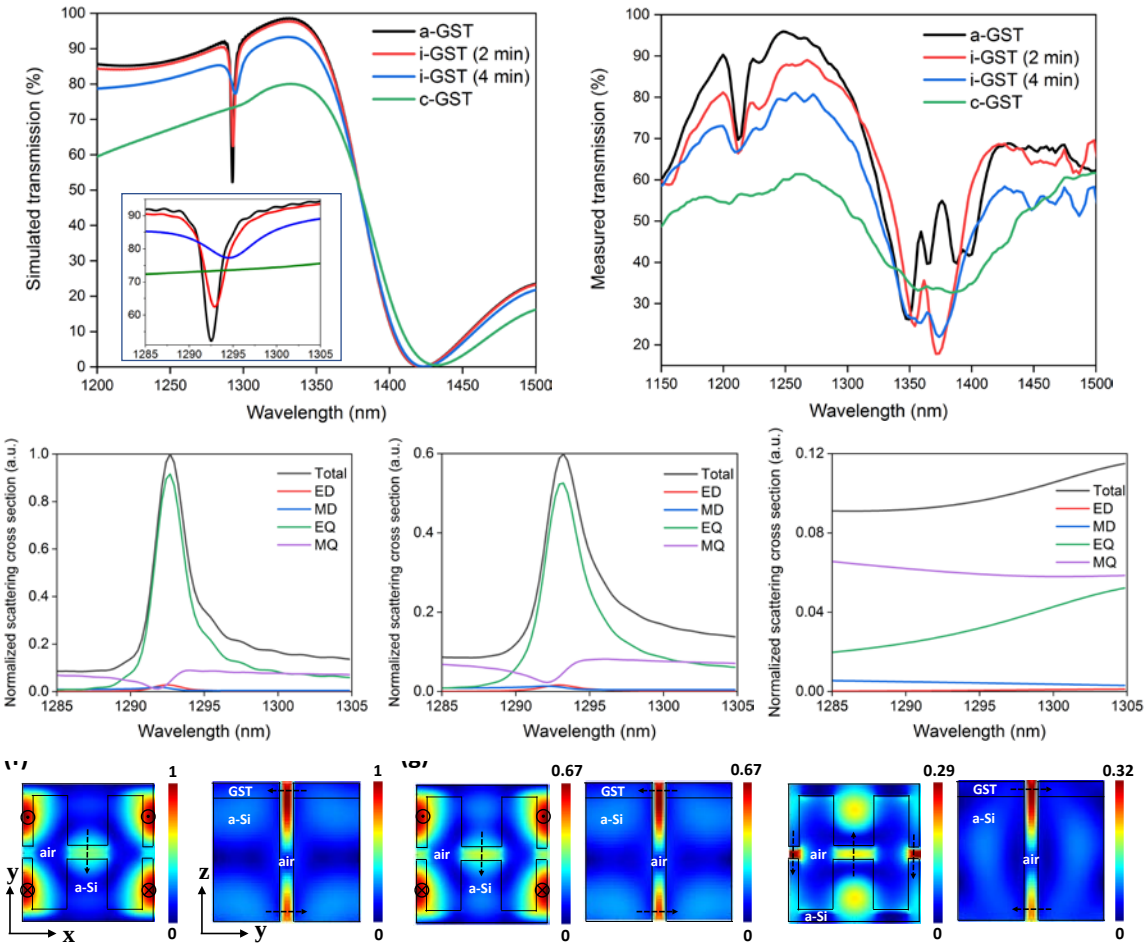

Figure 2. Hybrid silicon-GST nanostructure with tunable Fano-resonance. (a) Simulated transmission spectra of amorphous, intermediate states (annealing at 180 °C for 2 min and 4 min, respectively) and crystalline GST. (b) The corresponding measured transmission spectra for different states. Multipolar decomposition of one unit-cell of the proposed hybrid metasurfaces at (c) amorphous state, (d) intermediate state (2 min annealing time) and (e) crystalline state. Simulated normalized total electric field intensity for the cases of (f) a-GST, (g) i-GST (2 min) and (h) c-GST, respectively. For each sub-figure, the left plot for the horizontal plane at the position of z=200 nm, while the right plot for the vertical plane at the center of the proposed unit cell.

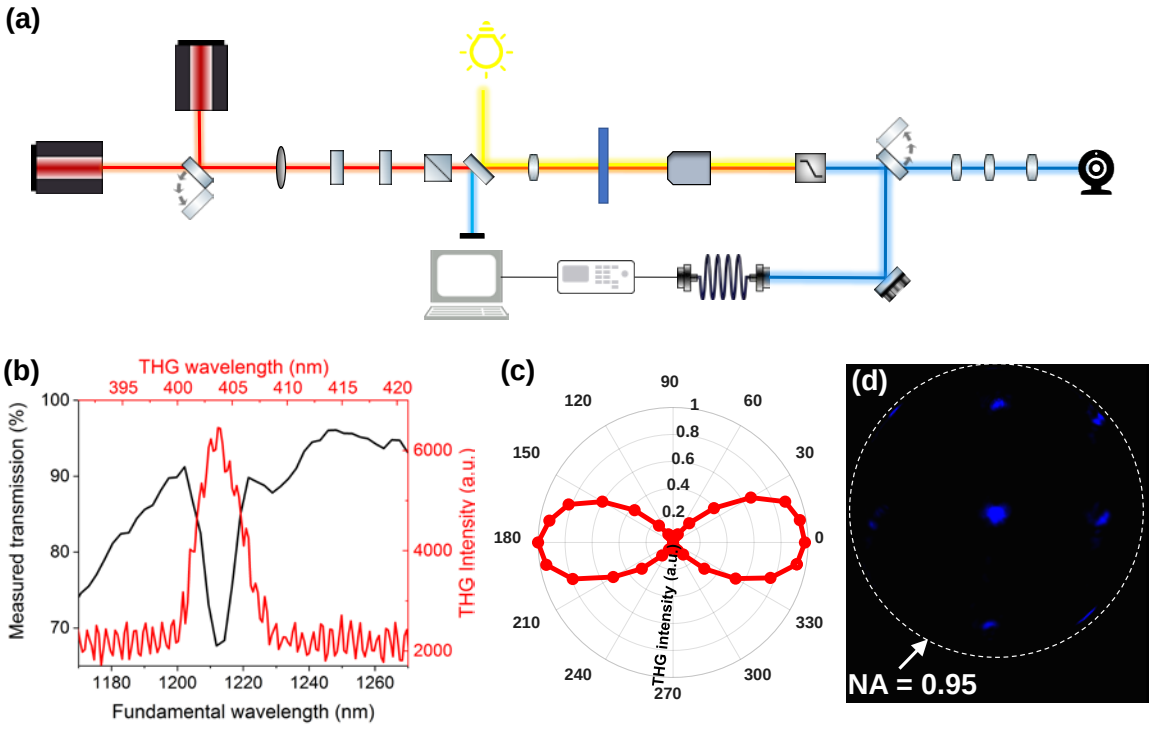

Figure 3. Optical characterization of THG emission at a-GST state. (a) Experimental optical setup used for transmission measurement of the proposed metasurfaces using ns-laser, THG power and spectrum using optical parametric oscillator laser, and back focal plane imaging of THG using 4f-telescope setup. (b) The measured transmission spectrum of the hybrid metasurfaces and the corresponding THG emission. (c) The normalized measured THG intensity versus the pump laser polarization. (d) Back focal plane imaging of the transmitted THG signal using an objective with high numerical aperture (NA = 0.95), showing a high concentration of the THG emission at the zero-order diffraction.

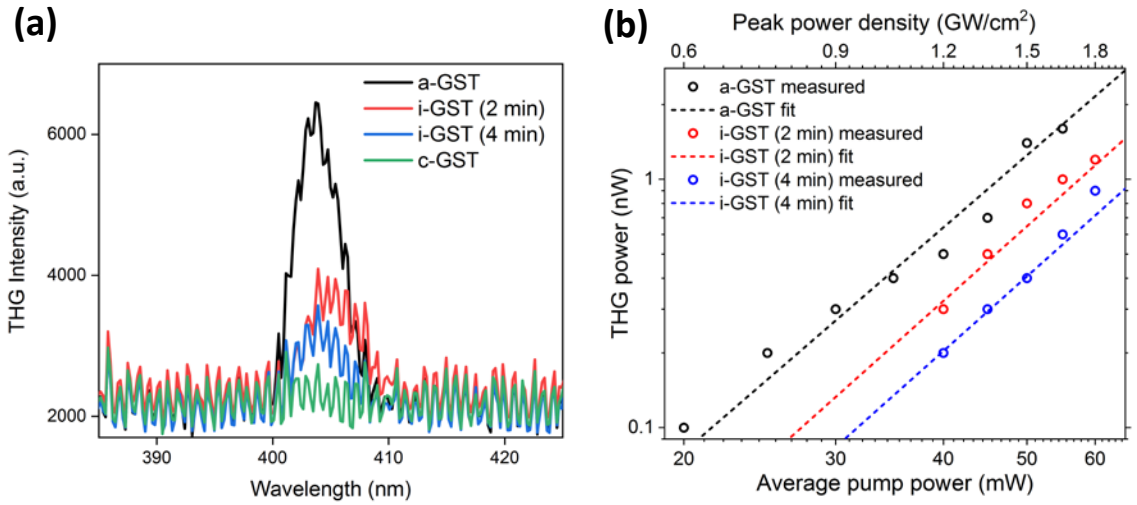

Figure 4. Tunable THG measurement and characterization. (a) Measured THG spectrum at different GST states. (b) The measured THG power in a log scale, slope of line fit set to 3 for a-GST, and line slope of 3.1 for i-GST (2 min) and (4 min) states.

REFERENCES

[1] Y. R. Shen, The Principles of Nonlinear Optics, John Wiley & Sons, New York, **1984**.

[2] D. Débarre, W. Supatto, A. M. Pena, A. Fabre, T. Tordjmann, L. Combettes, M. C. Schanne-Klein, E. Beaurepaire, *Nat. Methods* **2006**, 3, 47.

[3] R. W. Warren, L. C. Haynes, D. W. Feldman, W. E. Stein, S. J. Gitomer, *Nucl. Inst. Methods Phys. Res. A* **1990**, 296, 1-3.

[4] G. Hajisalem, M. S. Nezami, R. Gordon, *Nano Lett.* **2014**, 14, 11.

[5] H. Kishida, M. Ono, K. Miura, H. Okamoto, M. Izumi, T. Manako, M. Kawasaki, Y. Taguchi, Y. Tokura, T. Tohyama, K. Tsutsui, S. Maekawa, *Phys. Rev. Lett.* **2001**, 87, 177401.

[6] G. Sartorello, N. Olivier, J. Zhang, W. Yue, D. J. Gosztola, G. P. Wiederrecht, G. Wurtz, A. V. Zayats, *ACS Photonics* **2016**, 3, 8.

[7] F. Walter, G. Li, C. Meier, S. Zhang, T. Zentgraf, *Nano Lett.* **2017**, *17*, 3171.

[8] Z. Zeng, Y. Cheng, Y. Fu, X. Song, R. Li, Z. Xu, *Phys. Rev. A - At. Mol. Opt. Phys.* **2008**, 77, 023416

[9] M. S. Nezami, D. Yoo, G. Hajisalem, S. H. Oh, R. Gordon, *ACS Photonics* **2016**, 3, 8.

[10] J. Yu, S. Park, I. Hwang, D. Kim, J. Y. Jung, J. Lee, *Adv. Opt. Mater.* **2019**, 7, 1801510.

[11] A. Ahmadivand, M. Semmlinger, L. Dong, B. Gerislioglu, P. Nordlander, N. J. Halas, *Nano Lett.* **2019**, *19*, 605.

[12] S. M. Kamali, E. Arbabi, A. Arbabi, A. Faraon, *Nanophotonics*, **2018**, 7, 6.

[13] B. Sain, C. Meier, T. Zentgraf, *Advanced Photonics*, **2019**, 1, 024002.

[14] K. Koshelev, Y. Kivshar, *ACS Photonics*, **2020**, 8, 1

[15] M. R. Shcherbakov, D. N. Neshev, B. Hopkins, A. S. Shorokhov, I. Staude, E. V. Melik-Gaykazyan, M. Decker, A. A. Ezhov, A. E. Miroshnichenko, I. Brener, A. A. Fedyanin, Y. S. Kivshar, *Nano Lett.* **2014**, *14*, 6488.

[16] A. S. Shorokhov, E. V. Melik-Gaykazyan, D. A. Smirnova, B. Hopkins, K. E. Chong, D. Y. Choi, M. R. Shcherbakov, A. E. Miroshnichenko, D. N. Neshev, A. A. Fedyanin, Y. S. Kivshar, *Nano Lett.* **2016**, *16*, 4857.

[17] W. Tong, C. Gong, X. Liu, S. Yuan, Q. Huang, J. Xia, Y. Wang, *Opt. Express* **2016**, *24*, 19661.

[18] H. Liu, C. Guo, G. Vampa, J. L. Zhang, T. Sarmiento, M. Xiao, P. H. Bucksbaum, J. Vučković, S. Fan, D. A. Reis, *Nat. physics* **2018**, 14, 10.

[19] S. Zhang, G. C. Li, Y. Chen, X. Zhu, S. D. Liu, D. Y. Lei, H. Duan, *ACS Nano* **2016**, *10*, 11105.

[20] J. Qin, F. Huang, X. Li, L. Deng, T. Kang, A. Markov, F. Yue, Y. Chen, X. Wen, S. Liu, Q. Xiong, S. Semin, T. Rasing, D. Modotto, R. Morandotti, J. Xu, H. Duan, L. Bi, *ACS Nano* **2019**, *13*, 1213.

[21] G. Grinblat, Y. Li, M. P. Nielsen, R. F. Oulton, S. A. Maier, *Nano Lett.* **2016**, 16, 7.

[22] G. Grinblat, Y. Li, M. P. Nielsen, R. F. Oulton, S. A. Maier, *ACS Nano* **2017**, 11, 1.

[23] L. Xu, M. Rahmani, K. Zangeneh Kamali, A. Lamprianidis, L. Ghirardini, J. Sautter, R. Camacho-Morales, H. Chen, M. Parry, I. Staude, G. Zhang, D.

Neshev, A. E. Miroshnichenko, *Light Sci. Appl.* **2018**, 7,1.
[24] M. Semmlinger, M. Zhang, M. L. Tseng, T. T. Huang, J. Yang, D. P. Tsai, P. Nordlander, N. J. Halas, *Nano Lett.* **2019**, 19, 12.
[25] L. Carletti, K. Koshelev, C. De Angelis, Y. Kivshar, *Phys. Rev. Lett.* **2018**, 121, 033903.
[26] K. Koshelev, Y. Tang, K. Li, D. Y. Choi, G. Li, Y. Kivshar, *ACS Photonics* **2019**, 6, 7.
[27] A. P. Anthur, H. Zhang, R. Paniagua-Dominguez, D. A. Kalashnikov, S. T. Ha, T. W. W. Maß, A. I. Kuznetsov, L. Krivitsky, *Nano Lett.* **2020**, *20*, 8745.
[28] A. Nemati, Q. Wang, M. Hong, J. Teng, *Opto-Electronic Adv.* **2018**, 1, 180009.
[29] A. M. Shaltout, V. M. Shalaev, M. L. Brongersma, *Science*, **2019**, 364, 6441.
[30] D. Rocco, L. Carletti, R. Caputo, M. Finazzi, M. Celebrano, C. De Angelis, *Opt. Express* **2020**, *28*, 12037.
[31] M. R. Shcherbakov, K. Werner, Z. Fan, N. Talisa, E. Chowdhury, G. Shvets, *Nat. Commun.* **2019**, *10*, 1.
[32] G. Soavi, G. Wang, H. Rostami, D. G. Purdie, D. De Fazio, T. Ma, B. Luo, J. Wang, A. K. Ott, D. Yoon, S. A. Bourelle, J. E. Muench, I. Goykhman, S. Dal Conte, M. Celebrano, A. Tomadin, M. Polini, G. Cerullo, A. C. Ferrari, *Nat. Nanotechnol.* **2018**, 13, 7.
[33] N. Raeis-Hosseini, J. Rho, *Materials*, 2017, 10, 1046.
[34] F. Ding, Y. Yang, S. I. Bozhevolnyi, *Adv. Opt. Mat.* **2019**, 14, 1801709.
[35] S. Abdollahramezani, O. Hemmatyar, M. Taghinejad, H. Taghinejad, Y. Kiarashinejad, M. Zandehshahvar, T. Fan, S. Deshmukh, A. A. Eftekhar, W. Cai, E. Pop, M. A. El-Sayed, A. Adibi, *Nano Lett.* **2021**, *21*, 1238.
[36] F. Zhang, X. Xie, M. Pu, Y. Guo, X. Ma, X. Li, J. Luo, Q. He, H. Yu, X. Luo, *Adv. Mater.* **2020**, 32, 1908194.
[37] C. Ruiz De Galarreta, I. Sinev, A. M. Arseny, P. Trofimov, K. Ladutenko, S. Garcia-Cuevas Carrillo, E. Gemo, A. Baldycheva, J. Bertolotti, C. D. Wright, *Optica* **2020**, *7*, 476.
[38] T. Cao, K. Liu, Y. Tang, J. Deng, K. Li, G. Li, *Laser Photonics Rev.* **2019**, *13*, 1.
[39] Q. Lin, J. Zhang, G. Piredda, R. W. Boyd, P. M. Fauchet, G. P. Agrawal, *Appl. Phys. Lett.* **2007**, *91*, 10.
[40] P. Singh, P. Sharma, V. Sharma, A. Thakur, *Semicond. Sci. Technol.* **2017**, 32, 045015.
[41] M. F. Limonov, M. V. Rybin, A. N. Poddubny, Y. S. Kivshar, *Nat. Photonics* **2017**, *11*, 543.
[42] J. Zheng, A. Khanolkar, P. Xu, S. Colburn, S. Deshmukh, J. Myers, J. Frantz, E. Pop, J. Hendrickson, J. Doylend, N. Boechler, A. Majumdar, *Opt. Mater. Express* **2018**, 8, 6.
[43] E. Cho, S. Yoon, H. R. Yoon, W. Jo, *J. Korean Phys. Soc.* **2006**, *48*, 1616.
[44] B. Gholipour, J. Zhang, K. F. MacDonald, D. W. Hewak, N. I. Zheludev, *Adv. Mater.* **2013**, 25, 22.
[45] T. Yoshle, A. Scherer, J. Hendrickson, G. Khitrova, H. M. Gibbs, G. Rupper, C. Ell, O. B. Shchekin, D. G. Deppe, *Nature* **2004**, *432*, 200.
[46] Lumerical Inc. https://www.lumerical.com/products/, **2020**.
[47] R. Paniagua-Domínguez, Y. F. Yu, A. E. Miroshnichenko, L. A. Krivitsky, Y. H.

Fu, V. Valuckas, L. Gonzaga, Y. T. Toh, A. Y. S. Kay, B. Lukyanchuk, A. I. Kuznetsov, *Nat. Commun.* **2016**, 7, 1.